RESEARCH ARTICLE

The co-pyrolysis of waste urea–formaldehyde resin with pine sawdust: co-pyrolysis behavior, pyrocarbon and its adsorption performance for Cr (VI)

Wanzhen Zhong[1] · Xiaoteng Li[1] · Siyi Luo[1] · Weiqiang Tan[1] · Zongliang Zuo[1] · Dongdong Ren[1]

Abstract

Urea–formaldehyde (UF) resin is difficult to degrade and classified as hazardous organic waste. To address this concern, the co-pyrolysis behavior of UF resin with pine sawdust (PS) was studied, and the adsorption properties of pyrocarbon were evaluated with Cr (VI). Thermogravimetric analysis revealed that adding a small amount of PS can improve the pyrolysis behavior of UF resin. Based on the Flynn Wall Ozawa (FWO) method, the kinetics and activation energy values were estimated. It was observed that when the amount of UF resin exceeded twice that of PS, the activation energy of the reaction decreased, and they acted synergistically. The characterization of pyrocarbon samples showed that the specific surface area increased with the increase of temperature, while the content of functional groups showed the opposite trend. Intermittent adsorption experiments showed that $5UF + PS_{400}$ achieved 95% removal of 50 mg/L Cr (VI) at 0.6 g/L dosage and at pH 2. The adsorption process was consistent with the Langmuir isotherm and pseudo-second-order kinetics, and the maximum adsorption was 143.66 mg/g at 30 ℃. Furthermore, the adsorption process consisted of electrostatic adsorption, chelation, and redox reaction. Overall, this study provides a useful reference for the co-pyrolysis of UF resin and the adsorption capacity of pyrocarbon.

Introduction

Urea–formaldehyde (UF) resins are synthesized from the polymerization of formaldehyde and urea, and they are widely used as adhesives in aerospace, automotive, construction, and electronic industries owing to their excellent adhesion, wear resistance, corrosion resistance, and cost-effectiveness. In particular, UF resins have significantly contributed to the fabrication of synthetic panels in the construction industry, but the accumulation of waste resins, which are stable and difficult to biodegrade, poses serious environmental threats (Zhong et al. 2017). Until now, several

countries have classified waste resins as hazardous wastes, and European Union even enacted policies to ban the landfilling of these wastes (Girods et al. 2008; Piekarski et al. 2017).

Due to the high nitrogen content (15–25%) of UF, its direct incineration will release large amounts of harmful gases, such as ammonia, isocyanic and cyanic acids, and nitrogen oxides (Girods et al. 2008), further threatening health and environment. Therefore, incineration is not an economic and environmentally friendly treatment method for UF. The hydrolysis of UF resins is generally considered to be the reverse route of its synthesis reaction (Lubis and Park 2018). It has been reported that UF resins are more prone to hydrolysis in hydrothermal environments. However, the relevant studies supporting this claim are mainly focused on hydrolytic treatments using hydrochloric acid and formaldehyde (Liu et al. 2018; Ren et al. 2022), and the use of hazardous formaldehyde solutions for the degradation of UF resin residues is a harmful option to the environment. For this reason, pyrolysis, which can efficiently convert organic waste into higher-value chemical products, has received wide attention (Cesprini et al. 2020; Wang et al. 2020.

1 School of Environmental and Municipal Engineering, Qingdao University of Technology, No. 11, 777, Jialingjiang Rd, Huangdao District, Qingdao, Shandong 266033, People's Republic of China

In recent years, the control of the harmless degradation processes of UF waste resins and the enhancement of the quality of the products have garnered considerable research interest. It is found that the co-pyrolysis of UF resins with biomass mimics the synergistic effects between two independent pyrolytic processes, thereby improving the quality of the products (Liu et al. 2021).

The co-pyrolysis of urea–formaldehyde resin with pine sawdust displays certain interactions beyond just the superposition of two processes, so it is necessary to highlight the reaction mechanism and guide the control of realistic reaction conditions through thermogravimetric experiments and the calculations of the reaction kinetics. In addition, the functional properties of the constituent carbon are influenced by the co-pyrolysis conditions and the interactions between the two components. Also, the structures of pyrocarbons are modified by the interactions of the volatile matter generated during pyrolysis with chars (Liu et al. 2021; Vanreppelen et al. 2011). Pyrocarbons exhibit a wide range of promising applications in water treatment owing to their well-developed pores, extremely large specific surface area, and diverse surface chemistry. Therefore, the objectives of this work are (1) to clarify the co-pyrolytic interactions between waste urea–formaldehyde resin and pine sawdust; (2) to characterize the surface structures and chemical properties of the pyrocarbon products; (3) to reveal the adsorption properties and optimize the adsorption conditions of pyrocarbon on Cr (VI). To achieve the aforementioned objectives, the study combined the utilization of pyrolytic carbon resources with the treatment of metal ion pollution in an attempt to provide theoretical basis and data support for the harmless treatment of waste resins and high-value utilization in wastewater treatments.

Materials and methods

Materials

The UF resin in this investigation was extracted from a waste artificial board produced by a building decoration company in Jinan City, China. Pine sawdust (PS) was collected from a wood processing factory in Qingdao City, China. Firstly, the UF and PS were crushed through a 200 mesh (74 μm) sieve and dried in a blast oven for 12 h at 105 °C. The UF and PS were then thoroughly mixed in different ratios (*w/w*), namely, 5:1, 4:1, 3:1, and 2:1, and the resulting samples were

correspondingly named 5UF + PS, 4UF + PS, 3UF + PS, and 2UF + PS. Industrial characterization parameters, such as dry basis moisture (M_{ad}), ash (*A*), volatile matter (*V*), and fixed char (FC), of the UF and PS, were obtained based on the Chinese national standard GB/T 28731–2012. The elemental compositions of the materials were determined by an elemental analyzer (EA, Elementar vario, Germany), while the oxygen content was obtained by a difference method. The results are shown in Table 1. All chemicals used in this study were of analytical grade and all solutions were made with deionized (DI) water (18.2 MΩ), potassium dichromate (K_2Cr_2O7), sodium nitrate ($NaNO_3$), concentrated nitric acid (HNO_3), sodium hydroxide (NaOH), acetone (C_3H_6O), ethanol absolute (C_2H_6O), ethylenediaminetetraacetic acid disodium salt ($C_{10}H_{14}N_2Na_2O_8$), and diphenyl carbamide ($C_{13}H_{14}N_4O$) were purchased from Sinopharm Chemical Reagent Co. Ltd, Shanghai, China.

Thermogravimetric analysis

Thermogravimetry (TG) and differential thermogravimetry (DTG) were measured by the pyrolysis of UF resin, PS, and their four mixtures from 20 to 700 °C using a TG analyzer (NETZSCH 209F3) under a high-purity nitrogen (> 99.99%) environment at a heating rate of 20 °C/min. The DTG curve is the first-order derivative of the TG curve, which reflects the weight loss of a sample more intuitively. The gaseous products of the pyrolytic process were monitored online using an FTIR spectrophotometer (TENSOR 27, Bruker) in combination with a TG analyzer under high-purity nitrogen conditions. The temperature of the gas transport pipeline was kept at 200 °C to prevent condensation of the gaseous products. The FTIR spectra were obtained by continuous scanning in the wavenumber range of 4000–400 cm^{-1} at a resolution of 4 cm^{-1}, and the corresponding data were analyzed using the OMNIC 8.0 spectral analysis software.

Pyrolysis kinetic analysis

The activation energy of a reaction can be calculated using the TG data, which is an indicator of the difficulty of the pyrolysis process. However, a series of complex reactions were involved in the pyrolysis process, making it difficult

Table 1 Industrial and elemental analysis results of UF and PS

Sample	Industrial analysis (wt.%)				Elemental analysis (wt.%)				
	M_{ad}	A	V	FC	C	H	O	N	S
UF	9.78	13.8	74.17	2.25	33.64	5.61	29.59	17.36	0
PS	5.28	31.49	56.84	6.39	33.25	4.52	29.55	0.90	0.29

to determine the reaction mechanism, which necessitated the kinetic fitting analysis (Hu et al. 2007; Wang et al. 2019).

The solid pyrolysis reaction is shown as follows:

$$A \text{ (solid)} \rightarrow B \text{ (solid)} + C \text{ (gas)} \tag{1}$$
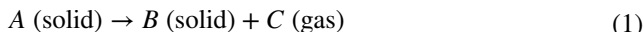
The mass loss of the solid can be expressed as

$$\alpha = \frac{w_0 - w_t}{w_0 - w_f} \tag{2}$$

where α is the degree of conversion, w_0 is the initial mass of the sample, w_t is the mass of the sample at time t, and w_f is the final mass of the sample.

The reaction rate is expressed as follows:

$$\frac{d\alpha}{dt} = kf(\alpha) = Ae^{\left(-\frac{E}{RT}\right)}f(\alpha) \tag{3}$$

where A is the prefactor (min^{-1}), E is the activation energy (J/mol), R is the universal gas constant (8.314 J/mol·K), T is the absolute temperature (K), and $f(\alpha)$ is the mechanism function that represents the reaction kinetics and depends on the reaction conditions.

Assuming a heating rate of $\beta = dT/dt$, we obtain

$$\frac{d\alpha}{f(\alpha)} = \frac{A}{B} \int_{T_0}^{T} e^{\left(-\frac{E}{RT}\right)} dT \tag{4}$$

Assuming $\alpha = \int_0^{\alpha} d\alpha/f(\alpha)$, we get

$$g(\alpha) = \int_0^{\alpha} \frac{d\alpha}{f(\alpha)} = \frac{A}{B} \int_{T_0}^{T} e^{-\frac{E}{RT}} dT \tag{5}$$

According to the Frank–Kameneskii approximation,

$$\int_{T_0}^{T} e^{-\frac{E}{RT}} dT = \frac{RT^2}{E} e^{-\frac{E}{RT}} \tag{6}$$

Applying the Coats–Redfern method for integration in Eq. (5), we get

$$\ln \frac{g(\alpha)}{T^2} = \ln\left[\frac{AR}{\beta E}\left(1 - \frac{2RT}{E}\right)\right] - \frac{E}{RT} \tag{7}$$

where $g(\alpha) = \int_0^{\alpha} \frac{d\alpha}{f(\alpha)}$ For the general temperature range and most E values, $\frac{E}{RT} \gg 1$; therefore, $1 - \frac{2E}{RT} \approx 1$.

The determination of an appropriate mechanism function, $f(\alpha)$ is the key step in kinetic research. According to previous studies, Table S1 depicts the mechanism functions in the pyrolysis of UF resins and cellulose, and n represents the number of reaction stages.

The plot of $\ln\left[g(\alpha)/T^2\right]$ against $1/T$ affords a straight line with a slope of $-\frac{E}{R}$. A higher linear correlation of the straight line indicates that the selected mechanism function, $f(\alpha)$ is more realistic. The line with the best fit was selected to evaluate the activation energy and the finger-front factor of the reaction.

Preparation and characterization of pyrocarbon

The UF and PS were crushed, passed through a 200-mesh sieve, and then mixed in different proportions and dried in square crucibles. Subsequently, the square crucibles were placed in a tube furnace (SJKJL-1200-II, Shanghai), whose temperature was raised to 400, 500, 600, and 700 °C at 20 °C/min under nitrogen atmosphere and kept for 30 min. The pyrocarbon prepared by the different ratios of UF and PS were named as 5UF + PS, 4UF + PS, 3UF + PS, and 2UF + PS.

The co-pyrolysis tests were performed in a tube furnace with the flow diagram as illustrated in Fig. 1. The chamber of the tube furnace was made of quartz tubes and was externally heated by an electric ring furnace, which was covered with an insulating layer on the outside. Porcelain boats with pyrolysis material were placed in the heating zone of the quartz tube, and the reflecting time and temperature were controlled by a smart controller. Nitrogen gas was introduced before each test to purge out oxygen. After the set pyrolysis time, the porcelain boats were pushed into the normal temperature zone for cooling before removal.

The morphology, porosity, functional groups, and surface charge of the pyrocarbon were analyzed by SEM (Quanta400, FEI), BET-specific surface area analysis (ASAP 2460, Micromeritics), and FTIR spectroscopy (iS50/6700, THERMO).

Adsorption of Cr (VI) on pyrocarbon

The effects of the adsorbent preparation parameters, adsorbent dosage and its components, and pH of the wastewater samples on the adsorption behavior of Cr (VI), including adsorption isotherms and kinetics and saturation adsorption
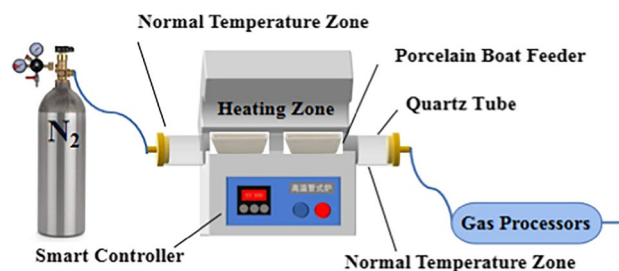

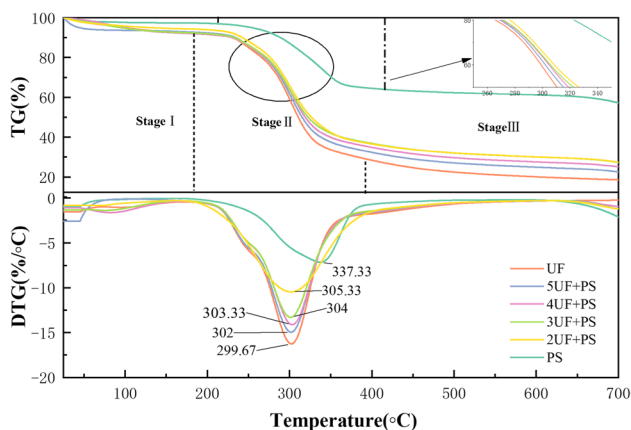**Fig. 1** Schematic diagram of the co-pyrolysis process

Fig. 2 TG and DTG curves of UF resin, PS, and their mixtures at a heating rate of 20 °C/min

capacity, were studied using simulating chromium-containing wastewater with potassium dichromate as the experimental object.

The adsorption experiment proceeded as follows: ethanol-washed pyrocarbon was added to 100 mL of 50 mg/L Cr (VI) solution. The sample was sealed and stirred in a shaking water bath at 150 rpm under a constant temperature of 20 °C for 90 min. Then, the mixture was passed through a 0.22-μm membrane and diluted, and the residual Cr (VI) content in the solution was measured by ultraviolet (UV) spectrophotometry.

The adsorption capability of pyrocarbon for Cr (VI) was calculated as shown:

$$Q_e = \frac{(C_0 - C)V}{m} \tag{8}$$

where Q_e and C are the adsorption capacity (mg/g) and concentration (mg/L) under adsorption equilibrium, respectively; m is the amount of adsorbent (g); C_0 is the initial concentration of Cr (VI) (mg/L); V is the volume of the solution (mL).

The primary adsorption mechanism in this study was investigated by adsorption kinetics and isotherm

experiments combined with SEM (Quanta400, FEI), BET (ASAP 2460, Micromeritics), and XPS (Axis Ultra DLD, Kratos) results.

Results and discussion

TGA analysis

Figure 2 shows the TG and DTG curves of UF resin, PS, and their different mixing ratios at a heating rate of 20 °C/min. The main reasons for the weight loss in each pyrolysis stage of UF and PS and the corresponding temperature ranges are listed in Table 2.

It is obvious that the pyrolysis processes of UF and PS were not synchronous, but had similar pyrolysis stages. The pyrolysis processes can be roughly divided into three weight-loss stages: dehydration and drying, rapid pyrolysis and volatile fraction removal, and slow charring of residual material.

The pyrolysis process of UF resin includes three main stages. The first stage had a mass loss of approximately 16%, which is mainly attributed to the removal of surface water and the release of free formaldehyde. In addition, previous studies reported that the condensation reaction of unreacted hydroxymethyl and amino groups can also lead to mass loss (Chen et al. 2021; Jiang et al. 2010; Roumeli et al. 2012). The second stage had a mass loss of approximately 70%, and this was mainly due to the dissociation of chemical bonds and the generation of volatile substances. The last stage was a slow charring process. PS exhibited a typical lignocellulosic biomass pyrolysis behavior. The pyrolysis process of PS is also divided into three stages: moisture removal, cellulose pyrolysis, and lignin cleavage, and the slow decomposition of residues (Guo et al. 2021).

By analyzing the TG-DTG curves in Fig. 2, the pyrolysis curves obviously shifted toward the UF end, and the maximum pyrolysis rate gradually increased with the increasing ratio of UF to PS. Previous studies showed the appearance of the maximum weight loss peak in the

Table 2 Temperature range and the main reasons for weight loss in each pyrolysis stage of UF and PS

	Sample	Temperature range (°C)	Main reasons of weight loss
I	UF	30–180	Evaporation of water and release of free formaldehyde
	PS	30–198	Evaporation of water and partial depolymerization
II	UF	180–396	Cellulose and lignin decomposition
	PS	198–416	Splitting of the terminal hydroxymethyl group, breaking of the C–N bond, and production of volatile substances
III	UF	396–700	Further decomposition of solid residues and condensation reaction of coke
	PS	416–700	

thermal decomposition curve of UF resin around 295 °C, while the pyrolysis temperature of PS was slightly higher than that of the UF resin, which may be due to the poor thermal conductivity of wood chips, causing the maximum thermal weight loss curve to shift toward the high temperature region (Feng et al. 2010). The higher the proportion of UF resin, the larger the shift of the maximum weight loss peak toward lower temperatures, thus verifying this conjecture. The initial pyrolysis temperature gradually decreased with the increasing ratio of UF resin to PS, which consequently decreased the pyrocarbon yield. In general, the following conclusions were derived: the UF resin had poor thermal stability and was extremely susceptible to pyrolysis. The pyrolysis performance was improved by the co-pyrolysis of UF with a small amount of PS.

Pyrolysis kinetic analysis

It is generally believed that the pyrolysis processes of high-temperature samples are mainly dependent on heat transfer rates rather than chemical reaction kinetics (Li et al. 2022). Therefore, the second stage of the TG curve was used as the region for linear fitting. The linear fitting results of the chemical reaction models with the diffusion control model using the Flynn–Wall–Ozawa (FWO) model are shown in Table S1, and the 3D diffusion model with the highest correlation coefficient was selected synthetically, i.e., when $f(\alpha) = 1.5(1-\alpha)^{2/3} [1-(1-\alpha)^{1/3}]^{-1}$, $G(\alpha) = [1-(1-\alpha)^{1/3}]^2$, and the fitting results of the activation energy, E and the finger front factor, A are shown in Table 3.

Activation energy is a crucial factor for examining the kinetic stability of materials, and it is used to reflect the amount of energy required for a chemical reaction (Chen et al. 2021). The activation energies for the thermal degradation of UF and PS calculated by the 3D diffusion model are 101.12 and 101.45 kJ·mol^{-1}, respectively. It is clear that the activation energy of PS was slightly higher than that of UF resin, indicating that more energy was required for the pyrolysis of PS.

The mixture of UF and PS at different ratios resulted in the occurrence of non-identical reactions in the pyrolysis stages, breakage of different chemical bonds, and ultimately causing differences in the activation energies of thermal degradation processes. Compared with the lone pyrolysis, the activation energies for the pyrolysis of 5UF+PS, 4UF+PS, and 3UF+PS samples were reduced, indicating that the co-pyrolysis process of the two components led to a synergistic effect, and the synergistic effect increased with the UF ratio. PS exhibited low density and a loose structure; thus, the surface structure was loose under a certain co-blending proportion, which benefitted the pyrolysis reaction and reduced the activation energy (Li et al. 2022). Conversely, the ease of pyrolysis declined when the PS ratio was above a certain limit. Notably, the highest activation energy was recorded for the 2UF+PS sample.

Pre-exponential factor (A) is used to assess the effective number of collisions in activated molecules (Chen et al. 2021). An increase in the value of A indicates increased collisions and more complex surface reactions, and vice versa (Müsellim et al. 2018; Wang et al. 2019). It can be seen from Table 3 that the UF pyrolysis reaction process was more complex than that of PS. The decrease in the value of A with increasing PS proportion means that the reaction became simpler in the presence of PS. This may be due to the promotion of free radical reactions in the co-pyrolysis process, which greatly reduced energy consumption (Sun et al. 2019).

Characterization of mixed pyrocarbon

Determination of porosity by BET analysis

As shown in Table 4, the S_{BET} and V_{pore} of the pyrocarbon samples showed gradual decreasing trends with increasing proportion of UF resin. The carbon of UF resin samples had the smallest S_{BET} and V_{pore} values. This is because the volatile substances in the UF resin were much easier to condense

Table 4 Porosity parameters of different pyrocarbon

	S_{BET} (m²/g)	V_{pore} (cm³/g)	D_{pore} (nm)	D_{BJH} (nm)
UF$_{400}$	295.2	0.224	30.5	39.3
2UF+PS$_{400}$	563.5	0.483	34.3	37.7
3UF+PS$_{400}$	506.9	0.430	34.0	37.8
4UF+PS$_{400}$	468.8	0.397	33.9	37.8
5UF+PS$_{400}$	330.2	0.339	41.1	37.8
Used 5UF+PS$_{400}$	331.3	0.327	36.8	33.7
5UF+PS$_{500}$	368.7	0.368	34.5	37.6
5UF+PS$_{600}$	665.5	0.496	29.7	38.8
5UF+PS$_{700}$	809.0	0.654	32.3	37.9

Table 3 Pyrolysis kinetic parameters of UF resin, PS, and their mixtures

Sample	E (kJ·mol^{-1})	A (min^{-1})	Regression equation	R^2
UF	101.12	7.07×10^8	$y = -12163.38x + 5.28$	0.9904
PS	101.45	2.61×10^8	$y = -12202.38x + 4.29$	0.9848
5UF+PS	100.59	6.04×10^8	$y = -12099.35x + 5.13$	0.9907
4UF+PS	95.76	2.08×10^8	$y = -11518.33x + 4.12$	0.9894
3UF+PS	95.11	1.80×10^8	$y = -11440.64x + 3.99$	0.9905
2UF+PS	103.51	9.81×10^8	$y = -12450.68x + 5.59$	0.9935

with greater tar conversion chances during the pyrolysis process, thereby covering the solid surface and pores (Pan et al. 2021; Vyas et al. 2017). The S_{BET} and V_{pore} values of the pyrocarbon significantly increased when the pyrolysis temperature was increased from 400 to 700 °C. With increasing temperature, the sample continuously released volatile compounds, which greatly influenced the pore development (Zhang et al. 2020b); on the contrary, the D_{pore} slightly decreased due to the collapse of the carbon structures and the aggregation of residues (Liu et al. 2021). The D_{pore} of all the samples was in the range of 2–50 nm, which correspond to the mesoporous structure class, and the D_{BJH} remained relatively stable under the different mixing ratios and temperatures, which favored the adsorption of metal ions (Gao et al. 2021).

Surface morphology analysis by SEM

SEM was used to examine the surface morphologies and pore characteristics of the pyrocarbon samples, and as shown in Fig. 3, the results are consistent with the BET analysis results. Compared with the test at 400 °C, it was observed that the carbon surface had several small stacked particles with more loosed structure, finer particles, and better pore development at 700 °C. This may be attributed to the more complete pyrolysis at higher temperatures, which generated large numbers of volatile compounds to promote pore development (Yuan et al. 2019). The pyrocarbon of the UF resin had greater strength, irregular shape, and smaller specific surface area than the mixed samples, indicating that the
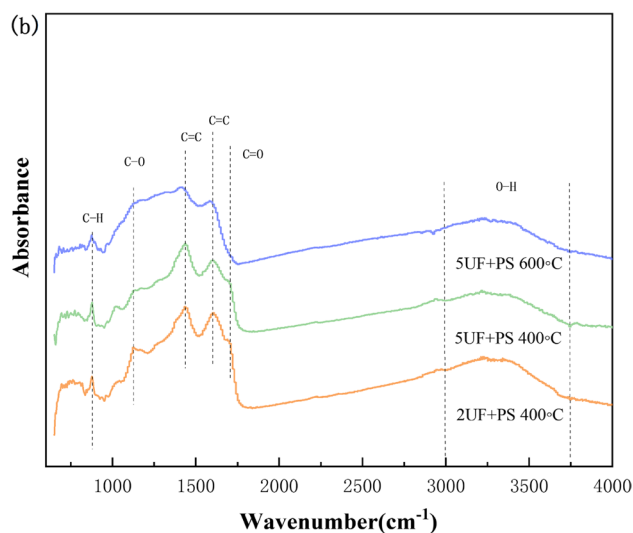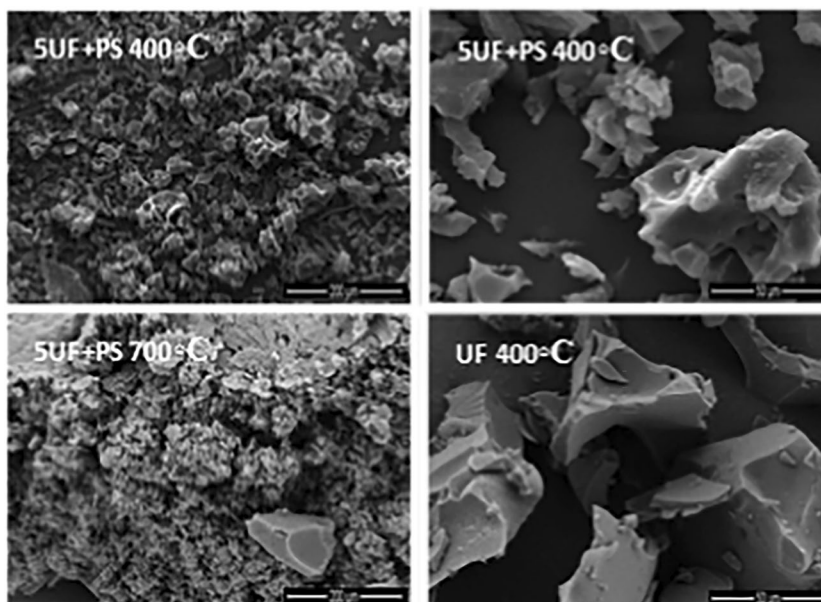
Fig. 4 FTIR spectra of the pyrocarbon samples

introduction of PS changed the pyrolysis behavior of the UF resin, rendering it more conducive to pore generation.

Surface functional groups of pyrocarbon

FTIR spectroscopy was used to verify the changes in the surface functional groups of the co-pyrocarbon samples. The appearance of several peaks in the FTIR spectrum confirmed the presence of various functional groups (carbonyl, carboxyl, hydroxyl, amide, etc.). As shown in Fig. 4, the peak at 3750–3000 cm^{-1} is attributed to the stretching vibration
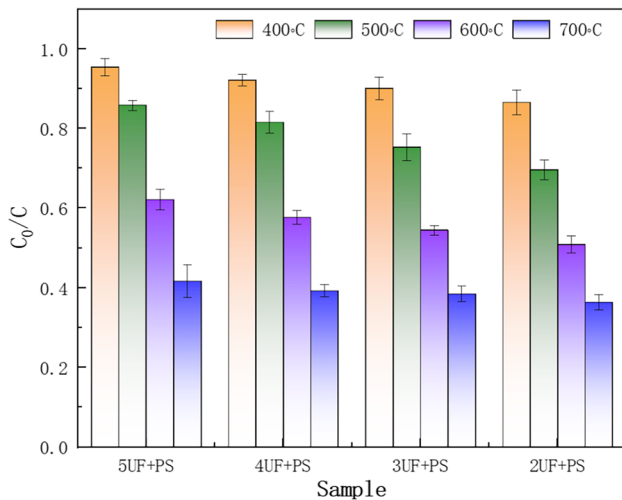

Fig. 3 SEM images of pyrocarbon prepared by UF and 5UF + PS at 400 and 700 °C

Fig. 5 Adsorption capacity of the pyrocarbon samples prepared at 400, 500, 600, and 700 °C for 50 mg/L Cr (VI) at a dosage of 0.6 g/L

(Liu et al. 2021). The peaks at 1580 and 1410 cm^{-1} are the stretching vibration peaks of C=C, where C=C in the aromatic ring is produced at 1580 cm^{-1}. The peak shape and intensity changed significantly with pyrolysis temperature and blending ratio, and both peaks shifted toward smaller wavenumbers at 600 °C, indicating that C=C existed in a more stable form (Zhang et al. 2020a). The peaks located between 1010–1270 cm^{-1} mainly correspond to the char chains and char-oxygen single bonds, and the peak at 880 cm^{-1} is ascribed to the generation of inward bending vibrations of unsaturated C–H, indicating that all the pyrocarbon contained unsaturated C and further verifying the generation of aromatic compounds (Li 2013).

Batch adsorption experiment of pyrocarbon

Comparison of the adsorption performances of the pyrocarbon samples

Figure 5 shows the performances of the pyrocarbon samples for the adsorption of 50 mg/L Cr (VI). The pyrocarbon samples were prepared by mixing UF and PS at different ratios, and pyrolysis was conducted at 400, 500, 600, and 700 °C. It is proven from previous studies that the adsorption capacity
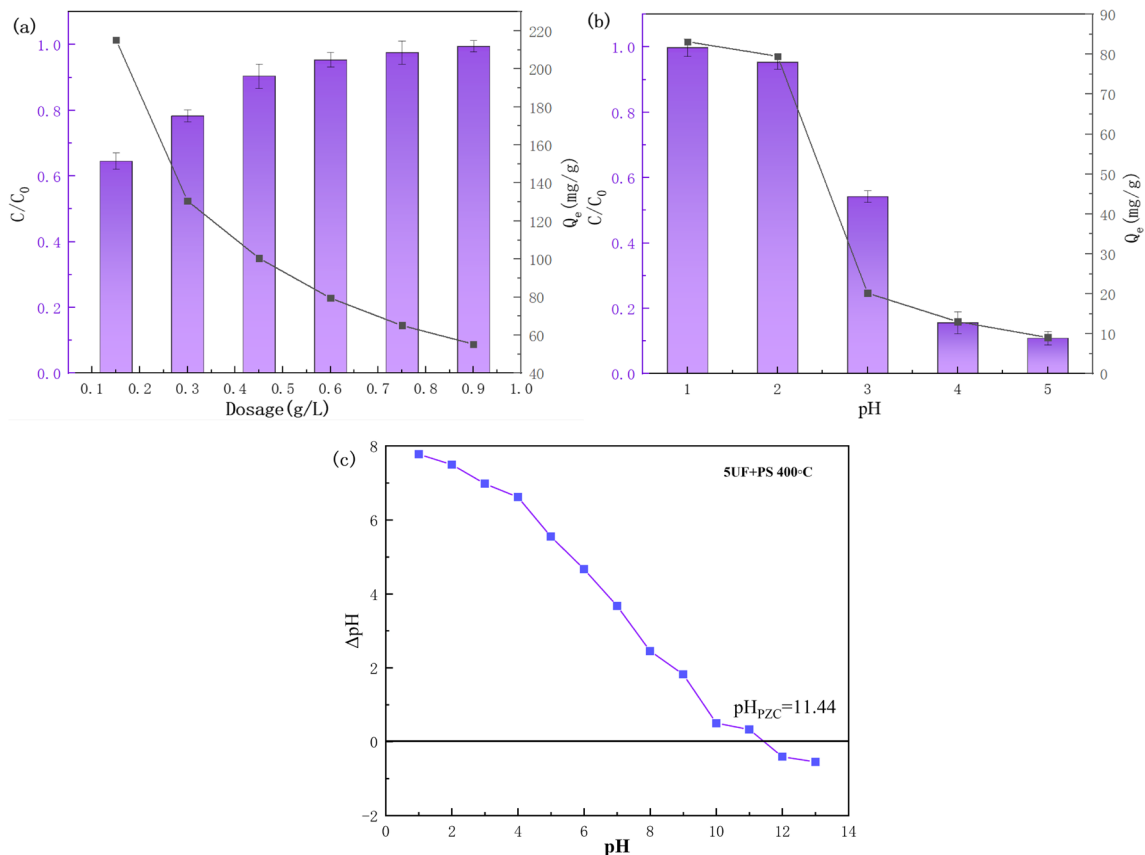
of O–H. The peak near 1690 cm^{-1} corresponds to the C=O stretching vibration, and it is found that the pyrolysis temperature had a significant effect on the C=O peak, meaning that temperature affects the formation of C=O compounds

Fig. 6 Effect of dosage (**a**) and pH (**b**) on the adsorption capacity of 5UF+PS$_{400}$ for 50 mg/L Cr (VI); pH$_{PZC}$ of 5UF+PS$_{400}$ (**c**)

Fig. 7 Adsorption isotherms and relevant fitting curves (**a**) and adsorption kinetics and relevant fitting curves (**b**) of Cr (VI) adsorption on 5UF+PS$_{400}$ at different concentrations
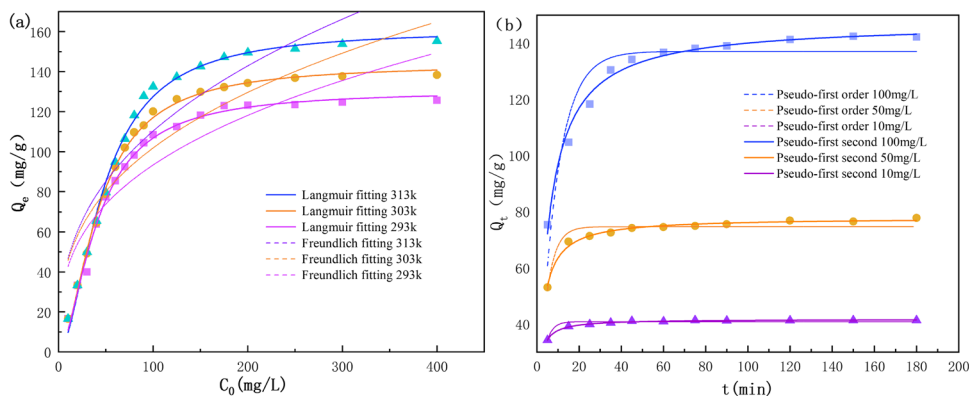
of pyrocarbon significantly decreases with increasing pyrolysis temperature. The increase in the pore size of the pyrocarbon did not show obvious effects on the enhancement of adsorption capacity. This indicates that the adsorption of Cr (VI) was dependent on certain functional groups. Due to the loss of functional groups, higher temperatures and longer pyrolysis durations led to a decrease in the adsorption efficiency, so it can be inferred that the adsorption of Cr (VI) on pyrocarbon is favored at lower temperatures (Yuan et al. 2011). In addition, the adsorption performance was improved at higher proportions of UF resin (high N content) in the mixture. This is because the N-containing functional groups facilitated the adsorption of Cr (VI) (Chen et al. 2017). Therefore, 5UF+PS$_{400}$ was chosen for the subsequent adsorption experiments on Cr (VI).

It can be seen from Fig. 6(a) that with increasing dosage of 5UF+PS$_{400}$ from 0.15 to 0.9 g/L, the adsorption efficiency for Cr (VI) rapidly increased from 64.5 to 99.5%, while the adsorption capacity decreased from 215.1 to 55.2 mg/g. The variation trends of adsorption capacity and removal rate become less pronounced when the dosage is above 0.6 g/L. This can be explained as follows: the adsorption process was mainly dependent on the contact between the effective adsorption sites on the pyrolyzed carbon and Cr (VI), and the effective adsorption sites were almost completely occupied at low dosage. The increase in dosage did not cause a significant improvement in the removal of Cr (VI), and this is attributed to the decrease in the utilization of adsorption sites (Liu et al. 2020), which led to an inverse ratio of water treatment cost to removal rate. Ultimately, 0.6 g/L was chosen as the optimum

dosage in this investigation, considering removal rate and cost-effectiveness.

As shown in Fig. 6(b), a pH range of 1–5 was set for examining the effect of pH on the adsorption of Cr (VI). Under these conditions, Cr (VI) mainly existed in the form of $HCrO_4^-$ and $Cr_2O_7^{2-}$ (Chen et al. 2017). The results show that the removal rate of Cr (VI) was more than 95% at pH 1–2, and it sharply decreased when the pH value increased above 2. As shown in Fig. 6(c), the zero charge point (pH$_{PZC}$) of 5UF+PS$_{400}$ was 11.44. Firstly, when the pH was lower than pH$_{PZC}$, the protonation effect on the adsorbent surface became significant and favored the adsorption of $HCrO_4^-$ and $Cr_2O_7^{2-}$. Notably, the adsorption capacity of the adsorbent was greatly improved at lower pH values. This is because the rates of H^+ release from the –COOH and –NH$_2$ functional groups were increased, as well as the exchange rate to the adsorbent surface, which facilitated the binding reactions to chromate (Kumar et al. 2018; Zhang et al. 2018). More importantly, the –NH$_2$ and –OH groups provided electrons for the partial reduction of Cr (VI) to Cr (III) during the adsorption process. Secondly, when the initial pH was higher than 2 (pH<pH$_{PZC}$), the introduction of the adsorbent raised the dilution of H^+ concentration, subsequently increasing the pH of solution. As a result, the surface protonation effect was weakened. At the same time, large amounts of anions, such as OH^- enhanced the competition with chromate. These explain the decrease in adsorption performance. Finally, the ionic form and quantity of Cr (VI) were also affected by pH. Moreover, increments in pH led to an increase in CrO_4^{2-}, and this

Table 5 Isotherm parameters for Cr (VI) adsorption on 5UF+PS$_{400}$

Temperature	Langmuir			Freundlich		
	Q_m (mg/g)	K_L (L/mg)	R^2	$1/n$	K_F mg$^{(1-n)}$L^n/g	R^2
293 K	130.60	0.0019	0.993	0.35	19.57	0.813
303 K	143.66	0.0015	0.996	0.34	20.57	0.815
313 K	161.02	0.0011	0.994	0.37	19.78	0.826

Table 6 Comparison of the adsorption capacity of different absorbents

Absorbent	Solution pH	Adsorption capacity (mg/g)	Reference
UF resin and PS co-pyrocarbon	2	143.66	This study
Maize bran	2	294.13	(Hasan et al. 2008)
Activated carbon prepared from almond shell	2	197.34	(Rai et al. 2018)
Phosphoric acid treated *Datura stramonium*	2	138.07	(Kumar et al. 2020)
Palm kernel shell	2	125	(Mehr et al. 2019)
Water caltrop (WC) shell	2	98.04	(Kumar et al. 2018)
Activated carbon prepared from *Cucumis melo* peel	3	97.96	(Manjuladevi et al. 2018)
Ocimum americanum L. seed pods	1.5	83.3	(Levankumar et al. 2009)

discourages Cr adsorption compared with $HCrO_4^-$ (Rai et al. 2018). Considering the applicability as well as the adsorption effect, the subsequent experiments were all performed at pH = 2.

Adsorption isotherms and kinetics

Figure 7(a) shows that the adsorption isotherms of $5UF + PS_{400}$ for Cr (VI) at 20, 30, and 40 °C exhibited typical "L" shapes, and the isotherm fitting parameters are listed in Table 5. Based on the R^2 values, the Langmuir model was more suitable than the Freundlich model for examining the adsorption of Cr (VI) by $5UF + PS_{400}$ at different temperatures. This indicates that the adsorption of Cr (VI) on $5UF + PS_{400}$ was monomolecular layer adsorption (Xiao et al. 2017). The equilibrium adsorption amount of Cr (VI) increased with increasing adsorption temperature, indicating that temperature increment is conducive for the adsorption of Cr (VI), and the adsorption process is an endothermic reaction. This may be explained as follows: higher temperatures facilitated the diffusion of Cr (VI) ions, making them more accessible to the adsorption sites. In addition, it activated the adsorbent, leading to the formation of new active sites and thus improving the adsorption performances (Zhou et al. 2016). The maximum adsorption capacity based on the Langmuir isotherm at 40 °C was 161.02 mg/g, which is higher than previously reported values, as listed in Table 6.

The kinetic fitting results are shown in Fig. 7(b) and Table 7. At the initial stage, a large number of active sites were present on the adsorbate surface, and they were readily bound to the adsorbent. Since the adsorption rate decreased, especially after 15 min, arising from the gradual decrease of the concentration gradient of Cr (VI) (adsorption driving force), the adsorption amount continued to increase gradually. This change may have been due to the gradual decrease in available adsorption sites. The adsorption amount was stabilized and finally attained equilibrium after 90 min due to the saturation of adsorption sites. Pseudo-secondary kinetic model fits the process better, and the adsorption process was effectively fitted to the quasi-secondary kinetic model, implying that chemisorption dominated the interactions between the adsorbent and the adsorbate (Aydın and Aksoy 2009; Liu et al. 2021). It can be seen from Table 7 that for the Webber–Morris model, the Q_e vs. $t_{1/2}$ fitted curve was not straight and did not pass through the origin ($C \neq 0$), so the adsorption rate was controlled by both membrane diffusion and intraparticle diffusion (Moussavi and Barikbin 2010).

Regeneration performance

Regeneration and reuse are important performance indicators for adsorbents. To investigate the repeated adsorption–desorption performances, the samples were collected after Cr (VI)

Table 7 Parameters fitted by kinetics and Webber–Morris model for Cr (VI) adsorption on $5UF + PS_{400}$

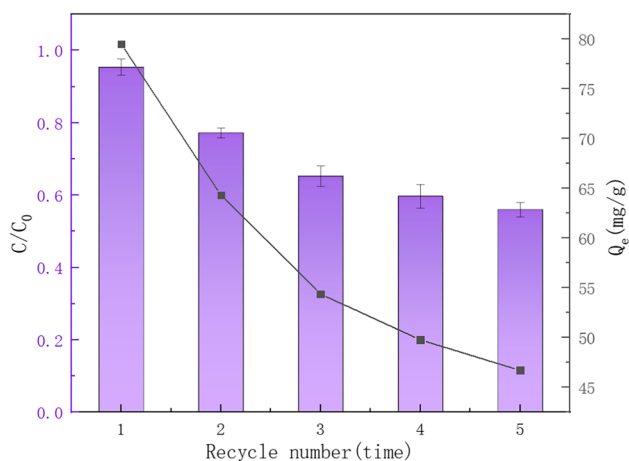| C_0 (mg/g)	Q_e (mg/g)	Pseudo-first order			Pseudo-second-order			Intra-particle diffusion		
		Q_m (mg/g)	k_1 (min^{-1})	R^2	Q_m (mg/g)	k_2 (g/mg/min)	R^2	K_i (mg/g/min$^{1/2}$)	C	R^2
25	41.3	40.85	0.363	0.902	41.76	0.02	0.994	0.43	36.81	0.534
50	77.8	74.68	0.239	0.905	77.89	0.0047	0.987	1.53	60.37	0.618
100	142.2	137.05	0.117	0.879	147.30	0.0015	0.985	4.95	88.74	0.703

Fig. 8 Adsorption capacity and removal rate of 50 mg/L Cr (VI) by 5UF+PS$_{400}$ after five cycles of adsorption–desorption experiments

adsorption and dried at 80 °C. Then, the desorption experiment was performed by adding the samples to 0.1 mol/L HCl solution and agitated for 12 h at 30 °C. After the desorption tests, the remaining HCl on the sample surface was washed with distilled water, followed by drying. After desorption, 5UF+PS$_{400}$ was again used for the adsorption of 50 mg/L Cr (VI) solution. The above steps were repeated five times.

As shown in Fig. 8, the regeneration study suggests that the adsorption capacity for the elimination of Cr (VI) decreased with the increasing number of regeneration cycles: 95.3% (1st), 77.2% (2nd), 65.3% (3rd), 55.7% (4th), and 56.1% (5th). This is attributed to the change in the functional groups on the regenerated absorbent surface and the fixation of some Cr (VI) in its pores (Kumar et al. 2018).

Mechanistic analysis of Cr (VI) adsorption on 5UF+PS$_{400}$

The XPS spectra of 5UF+PS$_{400}$ before and after the adsorption of Cr (VI) are shown in Fig. 9. The absorption peak of Cr 2p at 577 eV after adsorption on 5UF+PS$_{400}$ indicates that Cr (VI) was successfully adsorbed. In Fig. 9(b), the peaks at 576.4 (Cr 2p$_{3/2}$) and 586.1 (Cr 2p$_{1/2}$) eV correspond to Cr(III), while the peaks at 578.3 (Cr 2p$_{3/2}$) and 588 (Cr 2p$_{1/2}$) eV are attributed to Cr (VI) (Jain et al. 2010; Wang et al. 2015). The composition of Cr on the adsorbed 5UF+PS$_{400}$ surface was 50.77% Cr (III) versus 49.23% Cr (VI), demonstrating that most of the adsorbed Cr (VI) was reduced to Cr (III) (Zhao et al. 2016). The peak of N 1 s changed significantly, as displayed in Fig. 9(c) and (d). Specifically, the N 1 s peak at 398.6 eV shifted to 398.75 eV, while that at 400.2 eV

Fig. 9 XPS spectra of 5UF+PS$_{400}$ before and after adsorption of Cr (VI): **a** survey scan, **b** Cr 2p, **c** N 1s before adsorption, and **d** N 1s after adsorption
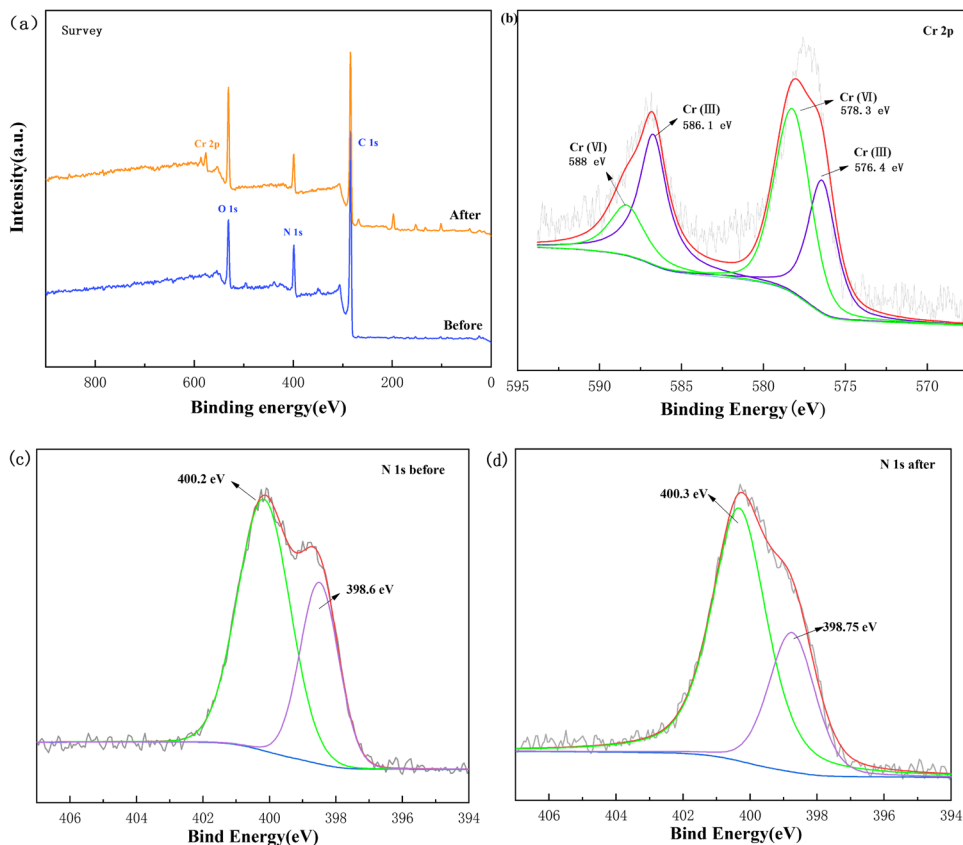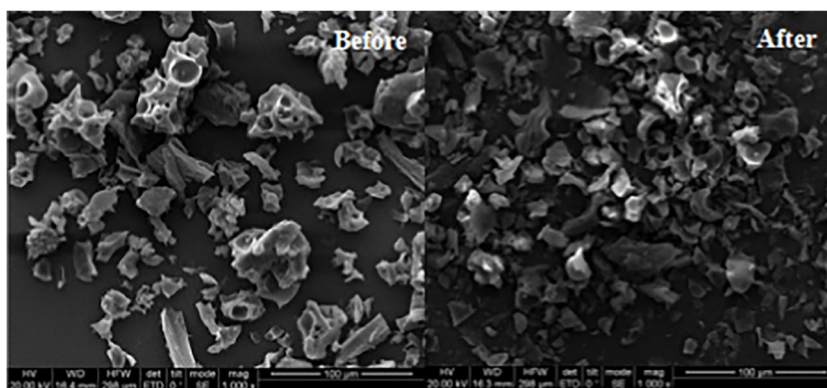
Fig. 10 SEM images of 5UF + PS$_{400}$ before and after adsorption of Cr (VI)

shifted to 400.3 eV. Moreover, there were also noticeable changes in the peak area, with the peak area at 400.2 eV decreasing from 78.8 to 65.7%. This is because the N atom in the amino or amide functional group provided electrons that immobilized Cr (III) after covalent bond formation, leading to chelation.

The SEM (Fig. 10) and BET (Table 4) analyses show that there were no obvious changes in the specific surface area and pore structures of 5UF + PS$_{400}$ before and after Cr (VI) adsorption. Therefore, it can be inferred that the internal pore channels of 5UF + PS$_{400}$ did not play key roles in the adsorption process of Cr (VI).

It has been proved that many organic functional groups can act as electron donors, and the surface of 5UF + PS$_{400}$ constituted some oxygen-containing functional groups, which benefitted the reduction of Cr (VI) (Kumar et al. 2018). The N-containing functional groups also played important roles in Cr (VI) adsorption. The –NH– and –NH$_2$

functional groups on the surface were protonated to –NH$_2^+$ and –NH$_3$, and these protonated forms can enhance adsorption by electrostatic attractions, thereby promoting the chelate effects (Chen et al. 2017; Kumar et al. 2020). Therefore, the mechanism of Cr (VI) adsorption on 5UF + PS$_{400}$ can be summarized as follows: Cr (VI) ions were adsorbed on the surface of 5UF + PS$_{400}$ by electrostatic attraction, and then they are immobilized by chelation and reduction reactions with functional groups, which supplied electrons to the surface of the adsorbent (Fig. 11).

Conclusions

(1) The pyrolysis experiments and kinetics analysis showed that the co-pyrolysis of UF resin with a small amount of PS improved the pyrolysis performances of the resin by reducing the activation energy, *E*. With the addition of PS, the pyrolysis weight loss peak moved slightly to the higher temperature zones, and the pyrocarbon yield was correspondingly increased.

(2) The carbon generated by co-pyrolysis had larger specific surface areas and abundant functional groups, which favored the adsorption process of a typical pollutant, Cr (VI).

(3) The batch adsorption experiments showed that the maximum removal rate of 95.33% and adsorption capacity of 142.2 mg/g for 50 mg/L Cr (VI) was achieved at a dosage of 0.6 g/L and pH of 2 using 5UF + PS$_{400}$ as adsorbent. The adsorption process was well comprehensively described by the Langmuir, pseudo-second-order, and Webber–Morris models. The adsorption was mainly driven by electrostatic attractions, chelation, and redox reactions.

(4) The carbon produced by the co-pyrolysis of UF resin and biomass has been verified to be a promising adsorbent in pollution control and resource recovery of acidic wastewater in mining, metallurgical, and electroplating industries.
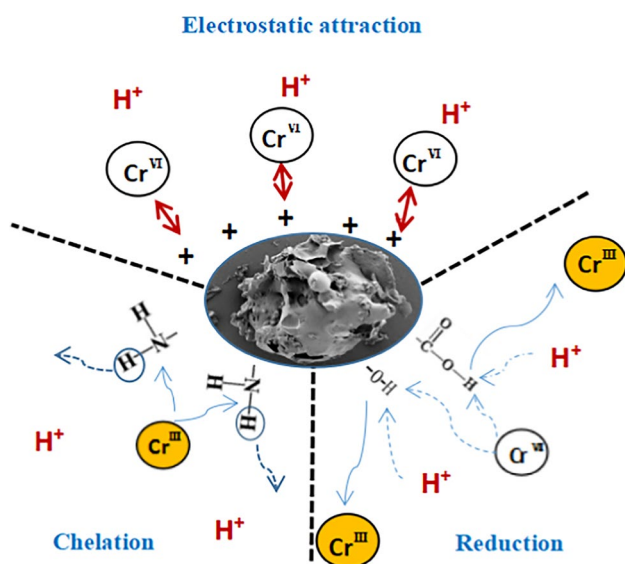

Fig. 11 Mechanisms of Cr (VI) adsorption on 5UF + PS$_{400}$

Author contribution Wanzhen Zhong: conceptualization, methodology, investigation, and writing—original draft. Xiaoteng Li: supervision and project administration. Siyi Luo: data curation and visualization. Weiqiang Tan: Software and resources. Zongliang Zuo: writing—review and editing. Dongdong Ren: validation and formal analysis.

Data availability All data generated or analyzed during this study are included in this published article [and its supplementary information files].

Declarations

Ethics approval and consent to participate Not applicable.

Consent for publication Informed consent was obtained from all individual participants included in the study.

Competing interests The authors declare no competing interests.

References

Aydın YA, Aksoy ND (2009) Adsorption of chromium on chitosan: optimization, kinetics and thermodynamics. Chem Eng J 151:188–194

Cesprini E, Resente G, Causin V, Urso T, Cavalli R, Zanetti M (2020) Energy recovery of glued wood waste – a review. Fuel 262:116520

Chen Y, de Oliveira LM, da Silva EB (2017) Mechanisms of metal sorption by biochars: biochar characteristics and modifications. Chemosphere: Environmental toxicology and risk assessment 178:466–478

Chen K, Cheng X, Chen Y, Qi J, Xie J, Huang X, Jiang Y, Xiao H (2021) Thermal degradation kinetics of urea–formaldehyde resins modified by almond shells. ACS Omega 6:25702–25709

Feng YS, Chen SH, Mu J (2010) Characterization of products from pyrolysis of waste wood-based composites containing urea-formaldehyde resins. Adv Mater Res 139–141:185–189

Gao L, Li Z, Yi W, Li Y, Zhang P, Zhang A, Wang L (2021) Impacts of pyrolysis temperature on lead adsorption by cotton stalk-derived biochar and related mechanisms. J Environ Chem Eng 9:105602

Girods P, Rogaume Y, Dufour A, Rogaume C, Zoulalian A (2008) Low-temperature pyrolysis of wood waste containing urea–formaldehyde resin. Renew Energy 33:648–654

Guo J, Ren X, Li S, Huang Z, Manzo M, Cai L, Chang J (2021) The impact of blending with poplar wood on the co-pyrolysis characteristics of waste particleboards [J]. Biomass Conversion and Biorefinery 13(6):4949–4956

Hasan SH, Singh KK, Prakash O, Talat M, Ho YS (2008) Removal of Cr (VI) from aqueous solutions using agricultural waste 'maize bran.' J Hazard Mater 152:356–365

Hu S, Jess A, Xu M (2007) Kinetic study of Chinese biomass slow pyrolysis: comparison of different kinetic models. Fuel 86:2778–2788

Jain M, Garg VK, Kadirvelu K (2010) Adsorption of hexavalent chromium from aqueous medium onto carbonaceous adsorbents prepared from waste biomass. J Environ Manage 91:949–957

Jiang X, Li C, Yong C, Yan J (2010) TG-FTIR study on urea-formaldehyde resin residue during pyrolysis and combustion. J Hazard Mater 173:205–210

Kumar S, Narayanasamy S, Venkatesh RP (2018) Removal of cr(vi) from synthetic solutions using water caltrop shell as a low-cost biosorbent. Sep Sci Technol 1–17

Kumar S, Shahnaz T, Selvaraju N, Rajaraman PV (2020) Kinetic and thermodynamic studies on biosorption of Cr(VI) on raw and chemically modified Datura stramonium fruit. Environmental Monitoring and Assessment 192

Levankumar L, Muthukumaran V, Gobinath MB (2009) Batch adsorption and kinetics of chromium (VI) removal from aqueous solutions by Ocimum americanum L. seed pods. J Hazard Mater 161:709–713

Li C-Z (2013) Importance of volatile–char interactions during the pyrolysis and gasification of low-rank fuels – a review. Fuel 112:609–623

Li XT, Bing HL, Luo SY, Zhang WW, Zuo ZL, Ren DD (2022) Study on the pyrolysis behaviors of urea-formaldehyde resin and rice straw mixed pellets. Frontiers in Energy Research 9:813114

Liu J, Yang X, Liu H, Cheng W, Bao Y (2020) Modification of calcium-rich biochar by loading Si/Mn binary oxide after NaOH activation and its adsorption mechanisms for removal of Cu(II) from aqueous solution. Colloids Surf A: Physicochemical and Engineering Aspects 601:124960

Liu J, Yang XY, Liu HH, Jia XP, Bao YC (2021) Mixed biochar obtained by the co-pyrolysis of shrimp shell with corn straw: co-pyrolysis characteristics and its adsorption capability. Chemosphere 282

Liu M, Wang Y, Wu Y, Wan H (2018) Hydrolysis and recycling of urea formaldehyde resin residues. J Hazard Mater 355:96–103

Lubis MAR, Park B-D (2018) Analysis of the hydrolysates from cured and uncured urea-formaldehyde (UF) resins with two F/U mole ratios. Holzforschung 72:759–768

Manjuladevi M, Anitha R, Manonmani S (2018) Kinetic study on adsorption of Cr (VI), Ni(II), Cd(II) and Pb(II) ions from aqueous solutions using activated carbon prepared from Cucumis melo peel. Appl Water Sci 8:36

Mehr MR, Fekri MH, Omidali F, Eftekhari N, Akbari-Adergani B (2019) Removal of chromium (VI) from wastewater by palm kernel shell-based on a green method

Moussavi G, Barikbin B (2010) Biosorption of chromium(VI) from industrial wastewater onto pistachio hull waste biomass. Chem Eng J 162:893–900

Müsellim E, Tahir MH, Ahmad MS, Ceylan S (2018) Thermokinetic and TG/DSC-FTIR study of pea waste biomass pyrolysis. Appl Therm Eng 137:54–61

Pan X, Gu Z, Chen W, Li Q (2021) Preparation of biochar and biochar composites and their application in a Fenton-like process for wastewater decontamination: a review. Sci Total Environ 754:142104

Piekarski CM, de Francisco AC, da Luz LM, Kovaleski JL, Silva DAL (2017) Life cycle assessment of medium-density fiberboard (MDF) manufacturing process in Brazil. Sci Total Environ 575:103–111

Rai MK, Giri BS, Nath Y, Bajaj H, Soni S, Singh RP, Singh RS, Rai BN (2018) Adsorption of hexavalent chromium from aqueous solution by activated carbon prepared from almond shell: kinetics, equilibrium and thermodynamics study. J Water Supply Res Technol AQUA 67:724–737

Ren T, Wang Y, Wu N, Qing Y, Li X, Wu Y, Liu M (2022) Degradation of urea-formaldehyde resin residues by a hydrothermal oxidation method into recyclable small molecular organics. J Hazard Mater 426:127783

Roumeli E, Papadopoulou E, Pavlidou E, Vourlias G, Bikiaris D, Paraskevopoulos KM, Chrissafis K (2012) Synthesis,

characterization and thermal analysis of urea–formaldehyde/nanoSiO2 resins. Thermochim Acta 527:33–39

Sun C, Li C, Tan H, Zhang Y (2019) Synergistic effects of wood fiber and polylactic acid during co-pyrolysis using TG-FTIR-MS and Py-GC/MS. Energy Convers Manage 202:112212

Vanreppelen K, Kuppens T, Thewys T, Carleer R, Yperman J, Schreurs S (2011) Activated carbon from co-pyrolysis of particle board and melamine (urea) formaldehyde resin: a techno-economic evaluation. Chem Eng J 172:835–846

Vyas A, Chellappa T, Goldfarb JL (2017) Porosity development and reactivity changes of coal–biomass blends during co-pyrolysis at various temperatures. J Anal Appl Pyrol 124:79–88

Wang H, Yuan X, Wu Y, Zeng G, Chen X, Leng L, Wu Z, Jiang L, Li H (2015) Facile synthesis of amino-functionalized titanium metal-organic frameworks and their superior visible-light photocatalytic activity for Cr (VI) reduction. J Hazard Mater 286:187–194

Wang B, Xu F, Zong P, Zhang J, Tian Y, Qiao Y (2019) Effects of heating rate on fast pyrolysis behavior and product distribution of Jerusalem artichoke stalk by using TG-FTIR and Py-GC/ MS. Renew Energy 132:486–496

Wang G, Dai Y, Yang H, Xiong Q, Wang K, Zhou (2020) A review of recent advances in biomass pyrolysis. Energy And Fuels 34:15557–15578

Xiao YL, Xue YW, Gao F, Mosa A (2017) Sorption of heavy metal ions onto crayfish shell biochar: effect of pyrolysis temperature, pH and ionic strength. Journal of the Taiwan Institute of Chemical Engineers 80:114–121

Yuan J-H, Xu R-K, Zhang H (2011) The forms of alkalis in the biochar produced from crop residues at different temperatures. Biores Technol 102:3488–3497

Yuan R, Yu S, Shen Y (2019) Pyrolysis and combustion kinetics of lignocellulosic biomass pellets with calcium-rich wastes from agro-forestry residues. Waste Manage 87:86–96

Zhang C, Zhang Z, Zhang L, Li Q, Li C, Chen G, Zhang S, Liu Q, Hu X (2020a) Evolution of the functionalities and structures of biochar in pyrolysis of poplar in a wide temperature range. Biores Technol 304:123002

Zhang J, Jin J, Wang M, Naidu R, Liu Y, Man YB, Liang X, Wong MH, Christie P, Zhang Y, Song C, Shan S (2020b) Co-pyrolysis of sewage sludge and rice husk/ bamboo sawdust for biochar with high aromaticity and low metal mobility. Environ Res 191:110034

Zhang ZY, Gao TT, Si SX, Liu QZ, Wu Y, Zhou GW (2018) One-pot preparation of P(TA-TEPA)-PAM-RGO ternary composite for high efficient Cr(VI) removal from aqueous solution. Chemical Engineering Journal 343:207–216

Zhao T-T, Ge W-Z, Nie Y-X, Wang Y-X, Zeng F-G, Qiao Y (2016) Highly efficient detoxification of Cr (VI) by brown coal and kerogen: process and structure studies. Fuel Process Technol 150:71–77

Zhong R, Gu J, Gao Z, Tu D, Hu C (2017) Impacts of urea-formaldehyde resin residue on recycling and reconstitution of wood-based panels. Int J Adhes Adhes 78:60–66

Zhou JG, Wang YF, Wang JT, Qiao WM, Long DH, Ling LC (2016) Effective removal of hexavalent chromium from aqueous solutions by adsorption on mesoporous carbon microspheres. Journal of colloid and interface science 462:200–207